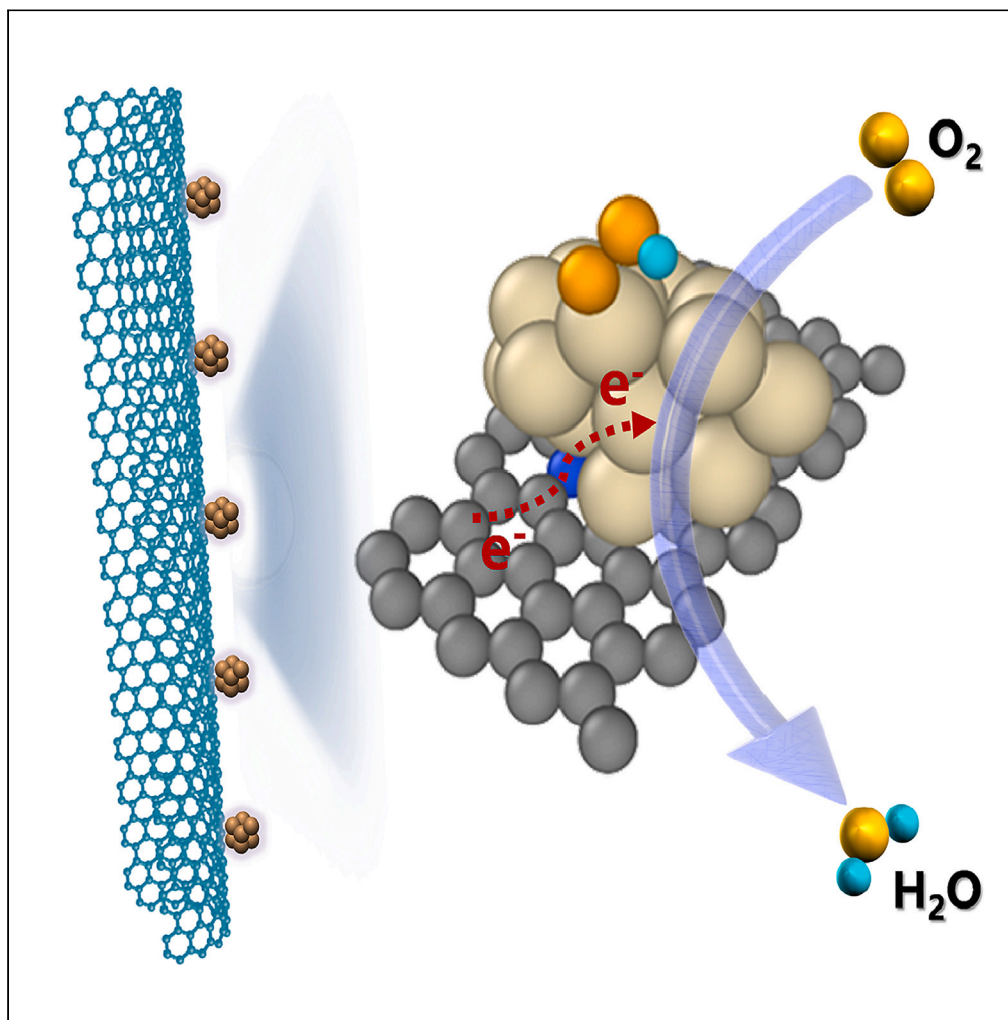


## Article

## Engineering carbon semi-tubes supported platinum catalyst for efficient oxygen reduction electrocatalysis



Jialin Cai,  
Junxiang Chen,  
Yizhe Chen, Jiujun  
Zhang, Shiming  
Zhang

smzhang@shu.edu.cn

**Highlights**

Semi-tubular Pt/N-CST  
catalyst is successfully  
constructed

Excellent activity and  
stability benefit from the  
Pt-N bond confirmed by  
EPR and XAFS

Interfacial Pt-N-C site  
provides a new active  
route for ORR  
electrocatalysis

Cai et al., iScience 26, 106730  
May 19, 2023 © 2023 The  
Author(s).  
[https://doi.org/10.1016/  
j.isci.2023.106730](https://doi.org/10.1016/j.isci.2023.106730)

## Article

## Engineering carbon semi-tubes supported platinum catalyst for efficient oxygen reduction electrocatalysis

Jialin Cai,<sup>1,3</sup> Junxiang Chen,<sup>2,3</sup> Yizhe Chen,<sup>1</sup> Jiuju Zhang,<sup>1</sup> and Shiming Zhang<sup>1,4,\*</sup>

## SUMMARY

**Innovation of catalyst structure is extremely important to develop the high-performance electrocatalysts for oxygen-reduction reaction (ORR). Herein, nitrogen-doped carbon semi-tube (N-CST) is used as a functional support for stabilizing the microwave-reduced Pt nanoparticles with an average size of ~2.8 nm to synthesize the semi-tubular Pt/N-CST catalyst. The contribution of interfacial Pt-N bond between N-CST support and Pt nanoparticles with electrons transfer from N-CST support to Pt nanoparticles is found by electron paramagnetic resonance (EPR) and X-ray absorption fine structure (XAFS) spectroscopy. This bridged Pt-N coordination can simultaneously help ORR electrocatalysis and promote electrochemical stability. As a result, the innovative Pt/N-CST catalyst exhibits excellent catalytic performance, realizing ORR activity and electrochemical stability superior to the commercial Pt/C catalyst. Furthermore, density functional theoretical (DFT) calculations suggest that the interfacial Pt-N-C site with unique affinity of O\* + OH\* can provide new active routes for the enhanced electrocatalytic ORR capacity.**

## INTRODUCTION

Hydrogen-fed proton exchange membrane fuel cells (PEMFCs) with advantages of high energy conversion efficiency, high energy/power densities, and environmental friendliness have been recognized as the next-generation energy conversion systems for electric vehicles.<sup>1</sup> However, their large-scale commercial applications are still in the stage of technology validation and demonstration. Some challenges are still needed to be overcome, including insufficient performance and reliability, high-price, and insufficient hydrogen fuel filling stations. One of the factors limiting the performance is insufficient electrocatalytic performance of catalysts, especially that of kinetically sluggish oxygen reduction reaction (ORR) at the PEMFC cathode due to the difficult activation/cleavage of O=O bond of oxygen.<sup>2</sup> Therefore, it is of great importance to develop high-performance catalysts for the ORR.<sup>3,4</sup> Currently, carbon black supported Pt nanoparticles (Pt/C) are still one type of the most practical catalysts although their catalytic activity and stability are not fully satisfied and price is relatively high.<sup>5–8</sup> To further achieve high catalytic ORR performance and reduce the cost by decreasing Pt loading, innovating the catalyst technology from the structural and composition design and material synthesis is necessary.

From the aspect of morphological structure, there are some improving rooms for granular Pt/C catalysts.<sup>9–12</sup> On the one hand, the weak binding between Pt nanoparticles and nanospherical carbon black is a shortcoming, which may result in the agglomeration and detachment of Pt nanoparticles as well as the reduction of both electrochemical active surface area and Pt utilization. It is expected that creating stronger chemical bond<sup>13–19</sup> and much more touchpoints<sup>20–22</sup> between metal nanoparticles and support through designing and synthesizing various nanostructured Pt-based alloy materials.<sup>23–25</sup> On the other hand, carbon black is inactive for ORR and susceptible to corrosion during ORR. It is needed to design innovative catalyst support materials with high bonding ability to metal catalyst nanoparticles and also being capable to resist the chemical/electrochemical corrosion.<sup>26–29</sup> In addition, the geometric structure of the commercial Pt/C catalyst is unordered. It is believed that designing catalysts with ordered structures could benefit mass transport in the catalyst layer to further improve performance of membrane electrode assembly.<sup>30–32</sup>

<sup>1</sup>Institute for Sustainable Energy/College of Sciences, Shanghai University, Shanghai 200444, China

<sup>2</sup>State Key Laboratory of Structural Chemistry, and CAS Key Laboratory of Design and Assembly of Functional Nanostructures, Fujian Institute of Research on the Structure of Matter, Chinese Academy of Sciences, Fuzhou, Fujian 350002, China

<sup>3</sup>These authors contributed equally

<sup>4</sup>Lead contact

\*Correspondence: smzhang@shu.edu.cn

<https://doi.org/10.1016/j.isci.2023.106730>



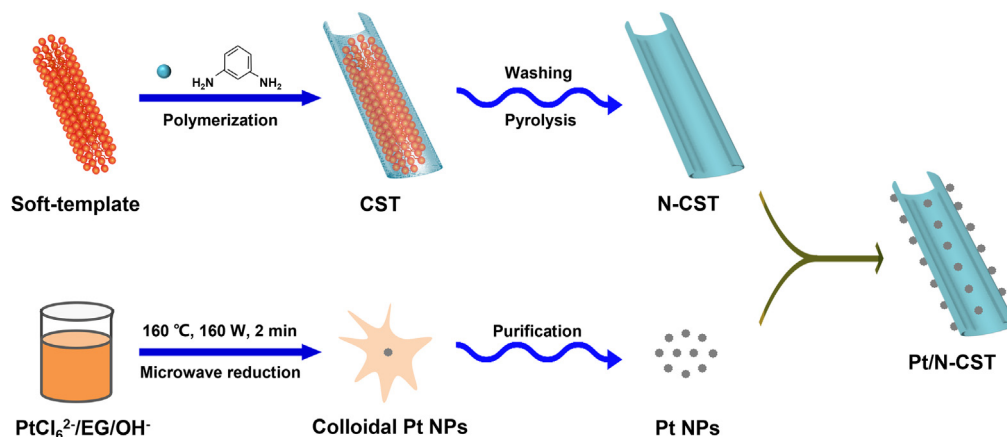


**Figure 1. Schematic illustration for the preparation of Pt/N-CST catalyst**

Although carbon-based materials have some shortcomings when used as the supports of Pt-based ORR catalysts, their important roles in achieving practical catalytic performance are obvious due to their high conductivity, large surface area, reasonable pore structure, and mechanical property.<sup>33</sup> Based on our previous explorations for carbon morphology,<sup>34,35</sup> this work employs a facile microwave reduction method for synthesizing the semi-tubular Pt-based catalyst. The synthesized N-doped carbon semi-tube (N-CST) support shows strong interaction and anchoring ability with Pt nanoparticles to form high-performance Pt/N-CST catalyst. As a semi-tubular nanostructure, N-CST can possess high specific surface areas, large pore volumes, abundant reaction sites, and gas diffusion channels. Moreover, N-doping can not only provide additional active sites for enhanced catalytic capability but also endow a strong Pt-support interaction for reinforced catalyst stability. An electron donation process can occur via the transfer of electrons from electron-rich N atoms to Pt nanoparticles. As a result, this unique semi-tubular carbon-supported catalyst exhibits superior ORR activity and stability than those of the commercial Pt/C catalyst.

## RESULTS

### Materials preparation and characterizations

The synthetic route of Pt/N-CST catalyst is illustrated in Figure 1. Typically, N-CST support can be first prepared through a combined polymerization-pyrolysis method as described in our previous studies.<sup>34,35</sup> In the polymerization process, the self-assembled one-dimensional micelle of cetyl trimethyl ammonium bromide (CTAB) dissolving in the water is acted as the soft-template, and the *m*-phenylenediamine (mPDA) molecules are used as the N and C sources. Once adding ammonium persulfates (APS), polymerization will occur in acidic condition for growing the CST which is pyrolyzed to obtain N-CST. Figure S1 shows the SEM images of CST and N-CST. As can be seen from Figure S1A, CST has a unique semi-tubular morphology of  $\sim 100$  nm in diameter. After carbonization, the as-prepared N-CST can still keep the semi-tube structure well but shrink in size with an average diameter of  $\sim 70$  nm (Figure S1B). Furthermore, N<sub>2</sub> adsorption-desorption isotherm (Figure S2A) demonstrates that N-CST has a higher Brunauer-Emmett-Teller (BET) surface area of  $1344.58 \text{ m}^2 \text{ g}^{-1}$  than that ( $\sim 250 \text{ m}^2 \text{ g}^{-1}$ ) of commercial Vulcan XC-72R carbon black.<sup>36</sup> Pore size distribution obtained by Barrett-Joiner-Halenda (BJH) method shows that there are abundant pore structures (Inset of Figure S2A). From X-Ray photoelectron spectroscopy (XPS) spectrum (Figure S2B) of N-CST support, three characteristic peaks of C, N, and O can be seen. The N-doping content in N-CST support is about 4.0 at%. As a catalyst support, the N-CST possesses large BET surface area, abundant pore structures, and high N-doping content, which can play key roles in high dispersion of Pt nanoparticles (NPs) and the strong interaction between Pt NPs and N-CST support. The synthesis of Pt NPs is done through microwave reduction of H<sub>2</sub>PtCl<sub>6</sub>·6H<sub>2</sub>O in alkaline ethylene glycol (EG) for the colloidal Pt NPs dispersion,<sup>37</sup> followed by purification with 1 M HCl solution. Further mixing Pt NPs suspension with N-CST support in ethanol, the expected Pt/N-CST catalyst can be obtained.

From the SEM image in Figure S3A, Pt/N-CST catalyst exhibits the intact semi-tubular morphology with the same as that of N-CST. Furthermore, the corresponding energy-dispersive X-ray spectroscopy (EDS) result (Figure S3B) provides the content of Pt in Pt/N-CST is 20.17 wt %. As shown in Figures 2A and S4, TEM

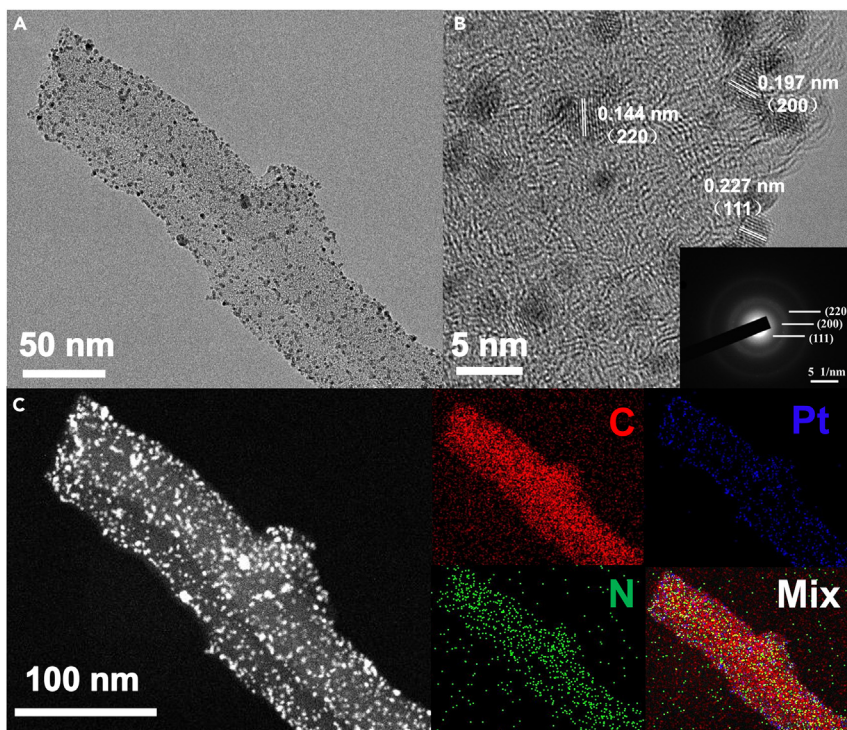


**Figure 2. Morphology characterizations of Pt/N-CST catalyst**

(A–C) TEM (A), HRTEM (B), and HAADF-STEM and the corresponding elemental mapping images of C, Pt, N (C).

images of the as-prepared Pt/N-CST catalyst show that Pt NPs are uniformly dispersed on the surface of N-CST support. The average diameter of Pt NPs is around 2.8 nm (Inset of Figure S4), slightly less than that of the commercial Pt/C catalyst (~3 nm). According to the HRTEM image (Figure 2B), the lattice fringe spacings of 0.234 nm, 0.140 nm, and 0.197 nm are respectively corresponding to the (111), (220), and (200) planes of Pt, which are well consistent with the electron diffraction pattern (Inset of Figure 2B). From the HAADF-STEM and elemental mapping images of Pt/N-CST catalyst (Figure 2C), the homogeneous distribution of C, Pt, and N can be observed.

Furthermore, Figure 3A shows XRD patterns of the as-prepared Pt/N-CST and commercial Pt/C catalyst. Their characteristic diffraction peaks are similar, originated from both carbon support, and face-centered cubic Pt crystal phase (JCPDS No.87-0636). Typically, the broad peak at approximately  $2\theta \approx 24.55^\circ$  can be assigned to the C(002) diffraction of the carbon supports, while the diffraction peaks located at  $2\theta \approx 39.48^\circ$ ,  $45.80^\circ$ ,  $67.37^\circ$ , and  $81.28^\circ$  are indexed to the (111), (200), (220), and (311) planes of Pt crystal, respectively. In order to study the composition and valence of elements in Pt/N-CST and Pt/C catalysts, the XPS tests were also carried out, as shown in Figure S5. It can be seen that there are three characteristic peaks of Pt, C, and O. Figure 3B shows high-resolution Pt 4f spectra of Pt/N-CST and Pt/C, which show two typical Pt 4f<sub>5/2</sub> and Pt 4f<sub>7/2</sub> peaks. These characteristic peaks can be divided into three paired Pt<sup>0</sup>, Pt<sup>2+</sup>, and Pt<sup>4+</sup>.<sup>38,39</sup> Compared with Pt/C, there is a negative shift (~0.3 eV) of Pt 4f binding energy for Pt/N-CST. The proportion of Pt<sup>0</sup> in Pt/N-CST is 58% which is higher than that of 48% in Pt/C. Moreover, Figure S6 exhibits the high-resolution O 1s spectrum of Pt/N-CST which can be deconvoluted into four characteristic peaks of oxygen-containing species, respectively corresponding to the Pt-O (531.5 eV), -C=O/C-OH (532.6 eV), -COOH (533.9 eV), and C-O-N (534.7 eV) structures.<sup>40–42</sup>

In addition, the signal of N can be found in Pt/N-CST when compared to Pt/C because of N-doping in the N-CST support. Notably, the high-resolution N 1s XPS spectrum of Pt/N-CST (Figure 3C) can be well divided into five peaks. Not only the pyridinic-N (398.3 eV, 11.7%), pyrrolic-N (400.2 eV, 21.7%), graphitic-N (401.1 eV, 36.4%), and oxidized-N (402.6 eV, 21.1%), but also a typical Pt-N bond (399.2 eV, 9.1%) can be observed, suggesting a strong interaction between N-doped support and Pt.<sup>43,44</sup> In order to further demonstrate the formation of Pt-N bond, the electron paramagnetic resonance (EPR) analysis

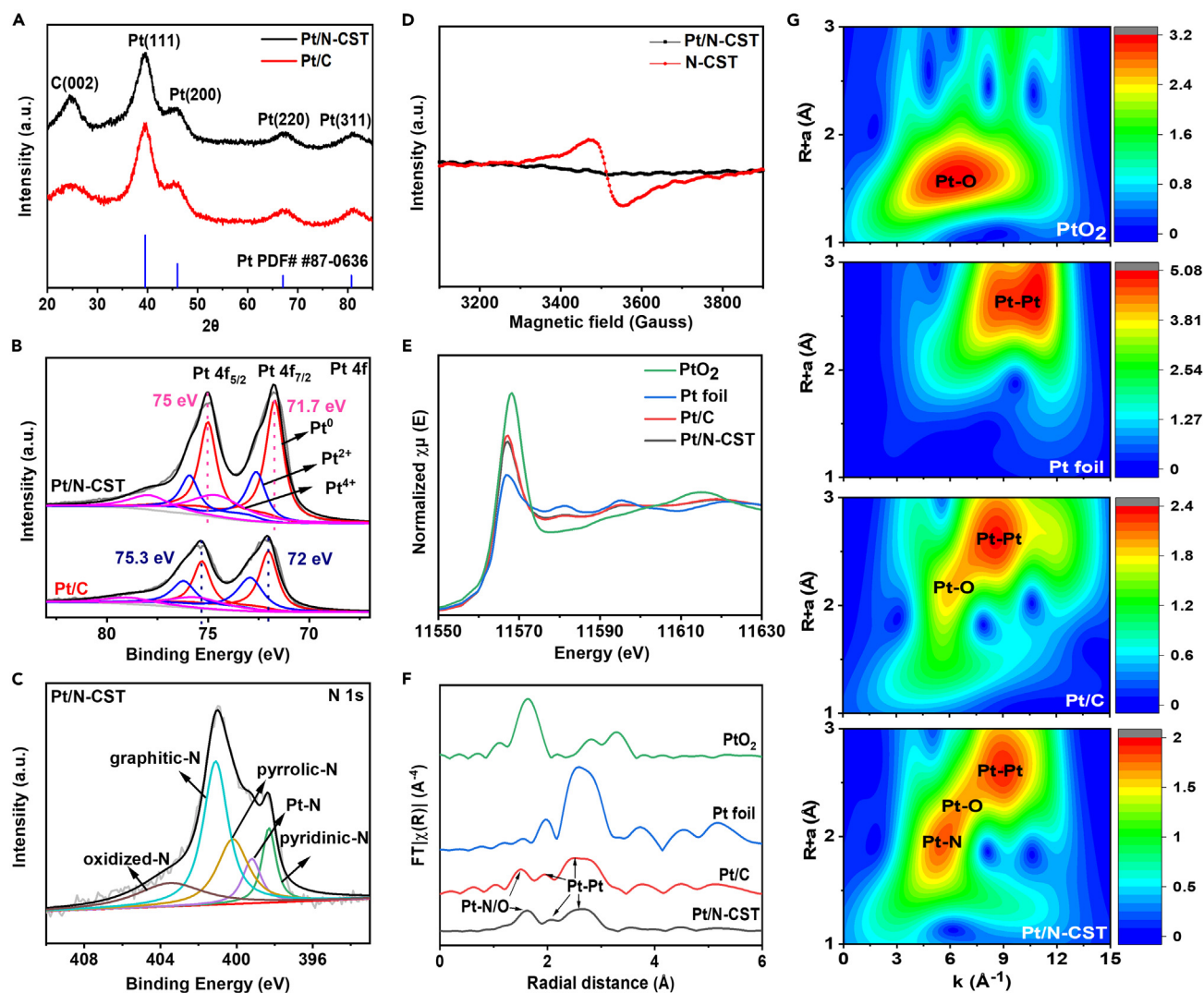


**Figure 3. Structure and composition analysis of the materials**

(A and B) XRD patterns (A) and high-resolution Pt 4f XPS spectra (B) of Pt/N-CST and Pt/C.

(C) High-resolution N 1s XPS spectrum of Pt/N-CST.

(D) EPR spectra of Pt/N-CST and N-CST.

(E–G) Pt L<sub>3</sub>-edge XANES spectra (E), the k<sub>3</sub>-weighted  $\chi(k)$ -function of the EXAFS spectra (F) and the wavelet transform of Pt L<sub>3</sub>-edge EXAFS data (G) for PtO<sub>2</sub>, Pt foil, Pt/C and Pt/N-CST.

was also carried out at room temperature (Figure 3D). The results show that the signal of Pt/N-CST is significantly reduced relative to that of N-CST. This is because a large amount of Pt NPs loaded on N-doped carbon support can cause a rapid relaxation of conduction electrons. This phenomenon may be attributed to the shift in the ground state electron cloud from N-CST support to Pt NPs through the interfacial Pt-N covalent attachment, induced by the stronger electron-withdrawing ability of these Pt NPs than the N-CST support.<sup>45,46</sup>

X-Ray absorption fine structure (XAFS) spectroscopy has been further employed to investigate the coordination environment and local electronic structure of Pt/N-CST and the obtained Pt L<sub>3</sub>-edge X-ray absorption near edge structure (XANES) are shown in Figure 3E. It can be obviously seen that the absorption edges of Pt/N-CST and Pt/C are located between Pt foil and PtO<sub>2</sub>. The white line (WL) intensity reflects the valence state of Pt. This result suggests that the Pt valence state of the two carbon-supported Pt catalysts should have fewer positive charges than PtO<sub>2</sub> but more than Pt foil. Also, the lower WL intensity of Pt/

**Table 1. EXAFS fitting parameters at the Pt L<sub>3</sub>-edge for various samples ( $S_0^2=0.86$ )**

Sample	Path	N <sup>a</sup>	R (Å) <sup>b</sup>	$\sigma^2$ (Å <sup>2</sup> ) <sup>c</sup>	$\Delta E_0$ (eV) <sup>d</sup>	R factor
Pt foil	Pt-Pt	12.0	2.76	0.0046	7.52	0.0057
PtO <sub>2</sub>	Pt-O	6.00	2.01	0.0032	11.22	0.0118
Pt/C	Pt-O	2.18	2.00	0.0065	1.19	0.0058
	Pt-Pt	7.06	2.75	0.0066	7.59	
Pt/N-CST	Pt-N	1.04	1.89	0.0081	8.89	0.0093
	Pt-O	2.38	1.99	0.0077	5.08	
	Pt-Pt	4.41	2.74	0.0091	1.98	

R factor indicates the goodness of the fit.

According to the experimental EXAFS fit of Pt foil by fixing N as the known crystallographic value.

<sup>a</sup>N, coordination number.

<sup>b</sup>R, distance between absorber and backscatter atoms.

<sup>c</sup> $\sigma^2$ , Debye-Waller factor to account for both thermal and structural disorders.

<sup>d</sup> $\Delta E_0$ , inner potential correction.

N-CST than Pt/C indicates the high proportion of Pt<sup>0</sup> in Pt/N-CST, consistent with the above XPS results (Figure 3B). This result confirms that N-doping can prohibit the oxidation of Pt.<sup>47</sup> Furthermore, Figure 3F shows the fourier transformed extended X-ray absorption fine structure (EXAFS) spectra of Pt L<sub>3</sub>-edge and the fitted results are shown in Figure S7. The corresponding fitting values of the structural parameters are listed in Table 1. For Pt/N-CST and Pt/C, the main peak at about 2.6 Å corresponds to the metallic Pt-Pt contribution, similar to the spectral distribution of Pt foil. The main Pt-O coordination can be found in commercial Pt/C at 1.5 Å. In addition to Pt-O contribution, there is a typical Pt-N bond in Pt/N-CST. As shown in Table 1, the average coordination number of Pt-N in Pt/N-CST is 1.04, which provides a direct evidence for the connection and bonding of Pt NPs with N-sites in carbon support. The wavelet transform spectra in Figure 3G show that there are two obvious intensities of Pt-Pt and Pt-O coordination in Pt/C. Although, an additional intensity contribution of Pt-N coordination can be found in Pt/N-CST. This is well in line with the corresponding curve fitting results.

### Electrocatalytic ORR performances

In order to obtain the optimal Pt/N-CST catalyst, the effects of microwave power (Figure S8), temperature (Figure S9), and time (Figure S10) on the electrochemical behavior of catalyst prepared by microwave reactor were studied. The results show that the best ORR activity can be achieved when the microwave power of 160 W, temperature of 160 °C and time of 2 min are set. Moreover, the parameters about the concentrations of NaOH (Figure S11) and H<sub>2</sub>PtCl<sub>6</sub> (Figure S12) have also been adjusted. As a result, 0.4 M of NaOH and 38.6 mM of H<sub>2</sub>PtCl<sub>6</sub> are the most suitable values. In addition, the order of adding carbon support in the catalyst synthesis process has also a great influence on Pt NPs dispersion behavior and electrochemical performance of the obtained catalysts. Taking the commercial Vulcan XC-72R carbon black as an example, if adding carbon support into the HCl-contained Pt NPs suspension before water washing, these Pt NPs with size of ~2.8 nm can have a good dispersion on the carbon support (Figure S13A). However, if carbon support is added after the beforehand water washing step, the Pt NPs will have severe aggregation (Figure S13B). Furthermore, the microwave-synthesized Pt/XC-72R catalyst obtained by adding carbon support before water washing has a larger cyclic voltammogram (CV) area and higher catalytic ORR activity with a half-wave potential ( $E_{1/2}$ ) of ~0.88 V (Figures S13C and S13D). This observation suggests that the HCl molecules can play a very important role in preventing Pt NPs from aggregating.<sup>48</sup>

Electrocatalytic performance of the optimal Pt/N-CST catalyst was investigated in 0.1 M perchloric acid (HClO<sub>4</sub>) solution using commercial Pt/C catalyst as baseline. According to the CV curves (Figure 4A), the larger electrical double-layer of Pt/N-CST than that of Pt/C can be ascribed to the high BET surface area of N-CST support (Figure S2A). The initial specific electrochemical active surface areas (ECSAs) can be calculated by integrating the charges collected in the H adsorption region (0.02–0.4 V) after double-layer correction with an assumption for H monolayer adsorption value of 210 μC cm<sup>-2</sup>. The ECSA of Pt/N-CST is 84.28 m<sup>2</sup> g<sub>Pt</sub><sup>-1</sup>, which is higher than that of the Pt/C (78.6 m<sup>2</sup> g<sub>Pt</sub><sup>-1</sup>). The larger ECSA value of Pt/N-CST may be due to the smaller size of Pt NPs with evenly dispersion on N-CST support. Figure 4B shows that the  $E_{1/2}$  occurs at ~0.89 V for the as-prepared Pt/N-CST catalyst, superior about 20 mV to that of the commercial

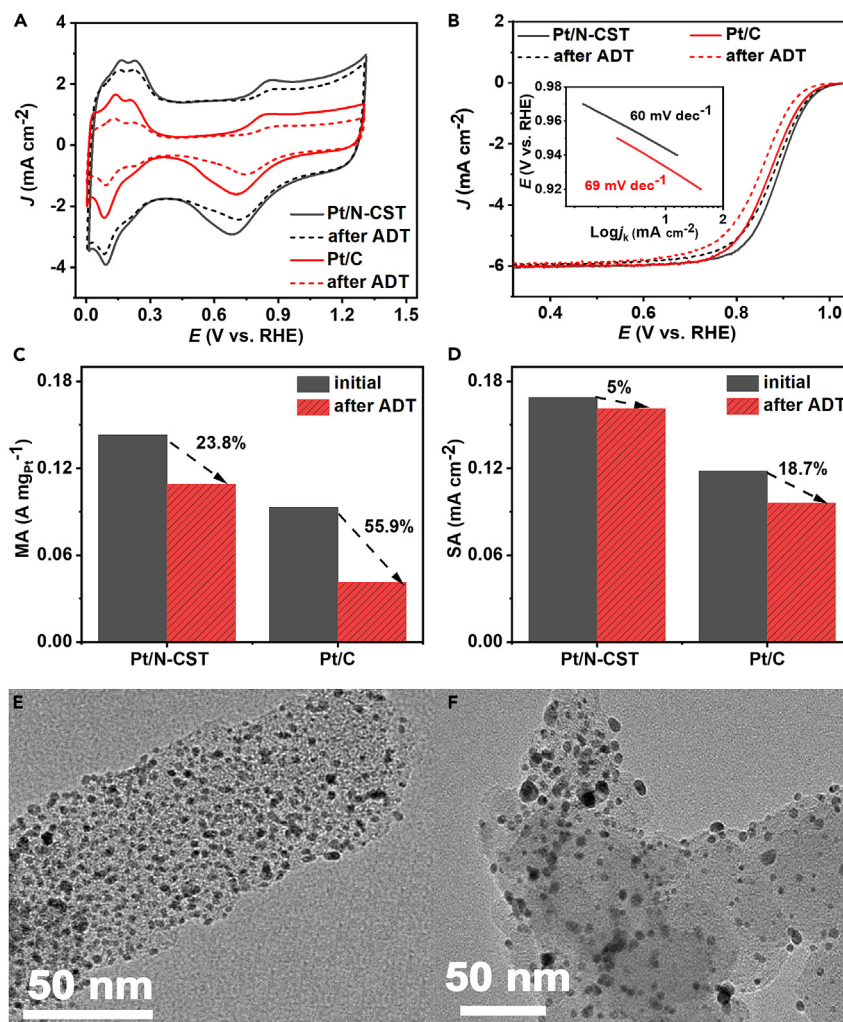


**Figure 4. Electrochemical performance of Pt/N-CST and Pt/C catalysts**

(A and B) CV (A), and ORR polarization curves and the corresponding Tafel plots and slopes (B) before (solid) and after (dotted) accelerated durability test (ADT).

(C and D) Mass activity (C) and specific activity (D) evolutions.

(E and F) TEM images of Pt/N-CST (E) and Pt/C (F) after ADT.

Pt/C catalyst ( $\sim 0.87$  V). By further comparison with other previously reported N-functional carbon-supported Pt-based catalysts, this characteristic Pt/N-CST exhibits the comparable catalytic performance with these excellent ORR catalysts (Table S1). Tafel slope of Pt/N-CST is  $60 \text{ mV dec}^{-1}$ , lower than that of Pt/C ( $69 \text{ mV dec}^{-1}$ ), indicating that Pt/N-CST has a faster ORR kinetics than Pt/C (Inset of Figure 4B). By using the Koutecky-Levich equation (Equation 1), the kinetic currents at  $0.9$  V can be extracted, which are  $0.858$  and  $0.558$  mA for Pt/N-CST and Pt/C, respectively. Subsequently, Figures 4C and 4D provide mass activity (MA) of  $0.143 \text{ A mg}_{\text{Pt}}^{-1}$  and specific activity (SA) of  $0.169 \text{ mA cm}^{-2}$  for Pt/N-CST, which are respectively  $\sim 1.5$  and  $\sim 1.4$  times higher than those of Pt/C ( $0.093 \text{ A mg}_{\text{Pt}}^{-1}$  and  $0.118 \text{ mA cm}^{-2}$ ), suggesting the improved activity due to the unique N-CST support.

To further understand the enhanced superior electrocatalytic capacity of Pt/N-CST catalyst, the electrochemical impedance spectroscopy (EIS) tests were carried out. The corresponding Nyquist plots of two Pt/N-CST and Pt/C catalysts are shown in Figure S14. Owing to the same electrochemical test system, there is a similar electrolyte solution resistance ( $R_s$ ) of  $\sim 1.2 \Omega$ . The diameter of Nyquist semicircle is positively correlated with the charge-transfer resistance ( $R_{ct}$ ) of oxygen reduction process from  $\text{O}_2$  to  $\text{H}_2\text{O}$ .<sup>49,50</sup> The typical  $R_{ct}$  values are about  $26.7$  and  $29.7 \Omega$  for the Pt/N-CST and Pt/C coated electrodes, respectively.

As well known, the fast charge and ion transfer is important for a good electrocatalyst. Therefore, the semi-tubular Pt/N-CST catalyst can be able to provide the improved ORR electrocatalysis compared with the granular Pt/C catalyst, which might be benefited from one-dimensional highly open structure and N-doping of semi-tubular morphology. Furthermore, we investigated the ORR capacity of two supports in acidic and alkaline electrolytes (Figure S15). As shown in Figure S15A, XC-72R is inactive for ORR but N-CST shows an  $E_{1/2}$  of  $\sim 0.67$  V in 0.1 M HClO<sub>4</sub> solution. When exploring in 0.1 M potassium hydroxide (KOH) solution (Figure S15B), N-CST can provide the  $E_{1/2}$  of 0.855 V. As a result, the  $E_{1/2}$  of prepared Pt/N-CST can reach to 0.904 V, which still exhibits higher catalytic ORR capacity than commercial Pt/C (0.876 V).

The electrochemical stability of catalysts has been evaluated by the accelerated durability test (ADT) through a continuous 10,000 potential cycles between 0.6 and 1.1 V in an O<sub>2</sub>-saturated 0.1 M HClO<sub>4</sub> solution. As shown in Figure 4A, the ECSA of Pt/N-CST catalyst after ADT is attenuated by 19.7% to reach 67.62 m<sup>2</sup> g<sub>Pt</sub><sup>-1</sup>, but that of Pt/C catalyst decreases to 42.8 m<sup>2</sup> g<sub>Pt</sub><sup>-1</sup>. Also, the  $E_{1/2}$  decline of Pt/N-CST catalyst is only 9 mV, whereas it is 28 mV for Pt/C catalyst (Figure 4B). Furthermore, the MA and SA of Pt/N-CST catalyst drop by 23.8% and 5%, respectively (Figures 4C and 4D). Comparatively, Pt/C catalyst shows much larger losses in MA (55.9%) and SA (18.7%). The above results show that the well-designed Pt/N-CST catalyst has a superior stability than the commercial Pt/C catalyst. After electrochemical stability tests, TEM analysis of the two catalysts was performed to check the morphological characteristics, structure, and particle size. As shown in Figure 4E, the morphology of Pt/N-CST catalyst is basically tenable, in which Pt NPs can maintain a uniform dispersion on the N-CST support although the average size becomes slightly larger ( $\sim 3.5$  nm). However, in the commercial Pt/C catalyst, the Pt NPs agglomerate seriously and the average particle size increases to  $\sim 5.5$  nm in diameter (Figure 4F). Moreover, the structure and composition of Pt/N-CST catalyst after ADT were further characterized by XRD and XPS. Figure S16A shows the XRD pattern with an increased intensity of main Pt (111) peak, which is caused by the slightly enlarged Pt NPs. As shown in Figure S16B, the Pt 4f result indicates a slight increase of Pt oxidation (44%) compared with the initial one (42%) from Figure 3B. As can be seen from N 1s XPS spectrum in Figure S16C, it remains the five typical N-species but with an obviously increased oxidized-N proportion (31.4%). The O 1s XPS spectrum in Figure S16D suggests that the electrochemical oxidation should mainly occur on the surface of carbon support from the obvious increase of -COOH proportion.

The above results suggest that the ORR performance enhancement in both catalytic activity and electrochemical stability for Pt/N-CST catalyst should be due to the N-doped semi-tubular support. For the improved catalytic activity, N-doping can create the additional ORR active sites like the high-efficiency pyridinic-N-C (carbon atoms next to pyridinic-N) and can also enhance the adsorption of oxygen and improve the conductivity of support.<sup>51–53</sup> Moreover, the covalent Pt-N bond at the interface of Pt NPs and N-CST support may act as the intermediate bridge of fast electron transfer and new ORR active site. For the enhanced electrochemical stability, there might be a possible reason that the uniform and sturdy insertion of such slightly smaller Pt NPs into the surface of carbon support with abundant pore structures.<sup>54</sup> More importantly, the deposition of Pt NPs on N-doped carbon support can make the formation of Pt-N bond, which results in more tenacious coordination of Pt NPs with N-CST support, thus enhancing the stability.<sup>55–57</sup>

### Theoretical calculations and mechanism exploration

First-principles density functional theoretical (DFT) calculations were also carried out to discuss the origin of the excellent ORR performance of Pt/N-CST catalyst. An ab initial molecular dynamics (AIMD) based annealing simulation to anchor an optimized Pt cluster onto an N-doped graphene was first executed. The constructed structure is shown in Figure 5A. This structure can generate three kinds of sites, namely, Pt site, N-C site, and Pt-N-C site in their interface. They are marked by orange, blue and green dashed frameworks in Figure 5A. And 3, 9, and 7 sites on the three kinds of surfaces were randomly sampled, respectively. Then the catalytic ORR by computational hydrogen electrode (CHE) method on these sites was calculated with the results plotted in Figure 5B.<sup>58</sup> The surfaces from the corresponding kinds of sites are marked by the same colors as those in Figure 5A. The associated individual free energy diagram (FED) and reaction intermediates are listed in Figures S17–S21. To analyze the ORR activity, a free-migration of adsorbate among the energy levels was assumed. As shown in the scheme of Figure 5C, there might be a possibility that reaction could take place firstly in N-C site, and then transfer to Pt site and Pt-N-C site to complete the whole reaction route. This massively happens in complex systems. By this free-migration assumption, the steps that have  $\Delta G_{\max} < 0$  (i.e., all the steps are turned exothermal) are plotted by dashed black lines. Those steps

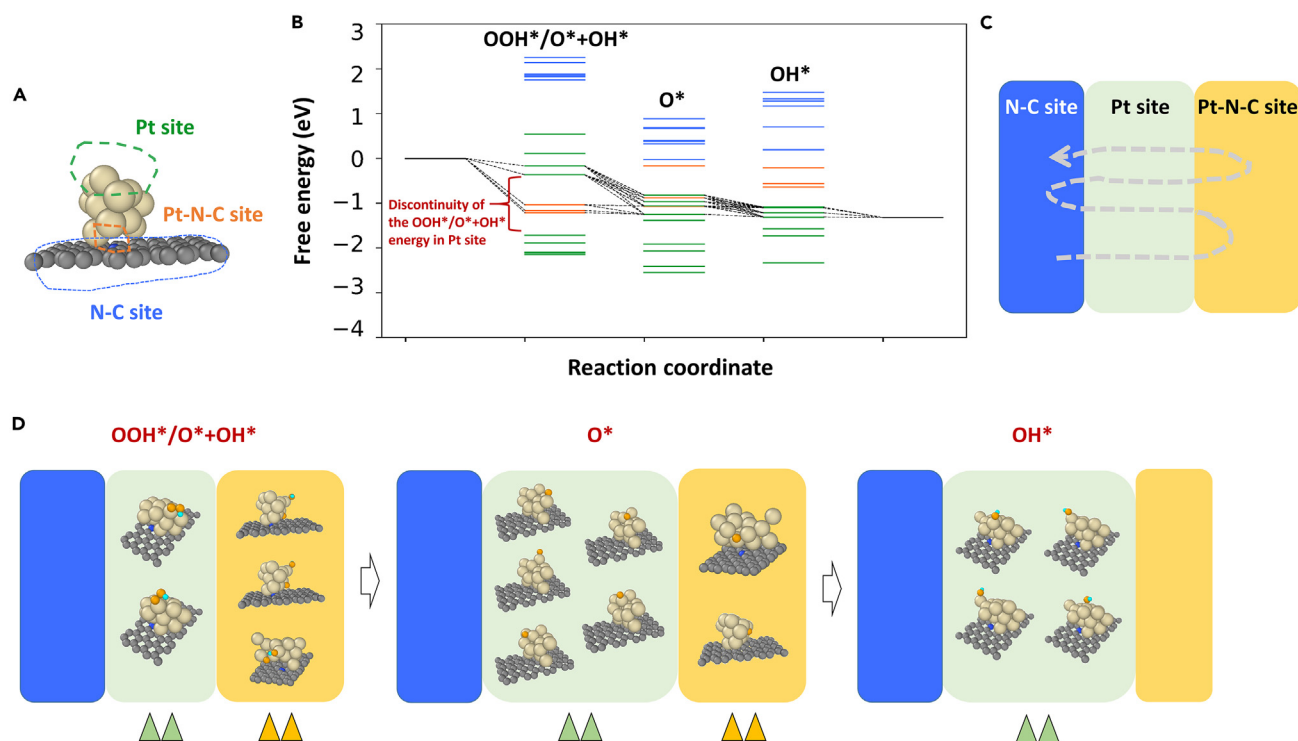


**Figure 5. Theoretical interpretation**

(A) The simulation model of Pt cluster onto N-doped graphene. Three kinds of sites are marked by three colors.

(B) The collected free-energy diagram (FED) of ORR on the possible sites. Black dashed lines indicate the step with  $\Delta G_{\max} < 0$ . The main adsorbates are used as the mark of the horizontal axis. Notice that the second adsorbate of the ORR process can either be OOH\* (R1a  $\rightarrow$  R2a) or O\*+OH\* (R1b  $\rightarrow$  R2b).

(C) Scheme of free-migration assumption of the adsorbate among phases.

(D) The optimized active structures of OOH\*/O\*+OH\*, O\*, and OH\*.

are the active routes that are responsible for the good ORR activity. The associated structures are listed in Figure 5D. It can be found that most active routes are consisted of the interfacial Pt-N-C site and Pt site, while those of N-C sites bind ORR intermediates weakly. Compared with Pt-N-C and Pt sites, Pt site can be alone as active site for ORR. The existence of Pt-N-C site can act as an important supplement of the Pt site, where all of the sites provide the optimized OOH adsorption sites (here the "OOH" means an intermediate step of ORR). The most of the Pt-N-C site binds optimally to O\*, with only one site binds too weak for O\*. However, the O\* site from Pt-N-C site cannot provide unique route such as that from OOH\*. Therefore, the role of Pt-N-C site can be interpreted as that it provides important additional OOH\* adsorption type for ORR, which improves the ORR activity.

It is important to note that the energy distribution of OOH\*/O\*+OH\* on Pt site is discontinuous, as marked in Figure 5B. If the optimal structures listed in Figures S17 and S18 are further analyzed, the cause of such a discontinuity should be due to the cracking of O-OH bond. Those cracked O-OH binds result in a stronger adsorption. The structures that are located above the discontinuity region all possess an unbroken OOH\*. This discontinuity is the very reason that some supplementary Pt-N-C sites for filling in this discontinuity is demanded. Moreover, the Pt-N-C sites are all with the cracked O-OH bonds, which have a weaker adsorption energy compared to the same Pt sites with O-OH broken bonds. This weaker adsorption energy is also seen in the adsorption of O\* and OH\*. This suggests that the presence of Pt-N-C site can weaken the reactivity of Pt site. So to recap, the interfacial Pt-N-C site with unique affinity of O\* + OH\* can provide new active routes for ORR, thus making an enhanced catalytic ORR activity.

## DISCUSSION

In summary, a characteristic support of N-doped carbon semi-tube (N-CST) has been successfully synthesized for the microwave reduction produced Pt nanoparticles to produce a Pt/N-CST catalyst. From the perspective of catalyst structure, the constructed Pt/N-CST can achieve a characteristic morphology with about 2.8 nm of Pt

nanoparticles uniformly deposited on the surface of N-CST support. Combining the experimental results of XPS, EPR, and XAFS tests with DFT calculations, a typical contribution of interfacial Pt-N coordination in Pt/N-CST catalyst for ORR is identified. Compared with the traditional Pt/C catalyst, the electronic transfer from N-CST support to Pt NPs can make a high proportion of metallic Pt in Pt/N-CST. The N-CST support can make the Pt-based catalyst manifold active sites, strong metal-support interaction, and sufficient mass transport, all of which together promote the catalytic ORR performances. As a result, the semi-tubular Pt/N-CST catalyst shows superior catalytic ORR activity with ~20 mV positive shift in half-wave potential than that of the commercial Pt/C catalyst and outstanding durability over 10,000 potential cycles.

### Limitations of the study

The semi-tubular catalyst is presented hoping to arouse wide interests for researchers in the fields of electrocatalysts, electrocatalysis, fuel cells, and so on. However, this study about the unique catalyst structure is just starting. More efforts should be done to design high-performance catalysts of Pt-based and non-precious metal by the further optimization of carbon semi-tube. Also, engineering more advanced semi-tubular electrocatalysts to achieve the real application in fuel cells remains a great challenge.

### STAR★METHODS

Detailed methods are provided in the online version of this paper and include the following:

- KEY RESOURCES TABLE
- RESOURCE AVAILABILITY
  - Lead contact
  - Materials availability
  - Data and code availability
- METHOD DETAILS
  - Preparation of N-CST support
  - Synthesis of Pt/N-CST catalyst
  - Physical characterizations
  - Electrochemical measurements
  - DFT calculations

### SUPPLEMENTAL INFORMATION

Supplemental information can be found online at <https://doi.org/10.1016/j.isci.2023.106730>.

### ACKNOWLEDGMENTS

This work was sponsored by the National Natural Science Foundation of China (Grant No. 22272105) and Natural Science Foundation of Shanghai (Grant No. 23ZR1423900). We would like to thank the Science Foundation of State Key Laboratory of Structural Chemistry (20210025), and Science Foundation of Fujian Province (2021J01526) for financial support.

### AUTHOR CONTRIBUTIONS

J.C. and J.C. contributed equally. J.C.: Methodology, data curation, investigation, writing – original draft. J.C.: Methodology, data curation, writing – review & editing, funding acquisition. Y.C.: Data curation, formal analysis. J.Z.: Formal analysis, writing – review & editing. S.Z.: Conceptualization, methodology, writing – review & editing, supervision, funding acquisition. All authors approved the final version of the manuscript.

### DECLARATION OF INTERESTS

The authors declare no competing interests.

Received: February 3, 2023

Revised: March 22, 2023

Accepted: April 19, 2023

Published: April 24, 2023

## REFERENCES

- Staffell, I., Scamman, D., Velazquez Abad, A., Balcombe, P., Dodds, P.E., Ekins, P., Shah, N., and Ward, K.R. (2019). The role of hydrogen and fuel cells in the global energy system. *Energy Environ. Sci.* **12**, 463–491.
- Chen, W., Xiang, Q., Peng, T., Song, C., Shang, W., Deng, T., and Wu, J. (2020). Reconsidering the benchmarking evaluation of catalytic activity in oxygen reduction reaction. *iScience* **23**, 101532.
- Zaman, S., Huang, L., Douka, A.I., Yang, H., You, B., and Xia, B.Y. (2021). Oxygen reduction electrocatalysts toward practical fuel cells: progress and perspectives. *Angew. Chem. Int. Ed.* **60**, 17832–17852.
- Chen, T., Ning, F., Qi, J., Feng, G., Wang, Y., Song, J., Yang, T., Liu, X., Chen, L., and Xia, D. (2023). PtFeCoNiCu high-entropy solid solution alloy as highly efficient electrocatalyst for the oxygen reduction reaction. *iScience* **26**, 105890.
- Tang, L., Xu, Q., Zhang, Y., Chen, W., and Wu, M. (2022). MOF/PCP-based electrocatalysts for the oxygen reduction reaction. *Electrochem. Energy Rev.* **5**, 32–81.
- Liu, H., Zhao, J., and Li, X. (2022). Controlled synthesis of carbon-supported Pt-based electrocatalysts for proton exchange membrane fuel cells. *Electrochem. Energy Rev.* **5**, 13.
- Zhang, S., Wang, Q., Dai, F., Gu, Y., Qian, G., Chen, C., Yu, Y., Yu, Y., and Zhang, J. (2021). Advanced noncarbon materials as catalyst supports and non-noble electrocatalysts for fuel cells and metal–air batteries. *Polymers* **13**, 336–381.
- Tang, M., Zhang, S., and Chen, S. (2022). Pt utilization in proton exchange membrane fuel cells: structure impacting factors and mechanistic insights. *Chem. Soc. Rev.* **51**, 1529–1546.
- Yu, X., and Ye, S. (2007). Recent advances in activity and durability enhancement of Pt/C catalytic cathode in PEMFC: Part I. Physico-chemical and electronic interaction between Pt and carbon support. *J. Power Sources* **172**, 133–144.
- Yu, X.T., Zhu, S.N., Xu, Z.D., Hu, X.Q., Zhu, T.F., Chen, J.Q., and Lu, S.L. (2007). Recent advances in activity and durability enhancement of Pt/C catalytic cathode in PEMFC: Part II: degradation mechanism and durability enhancement of carbon supported platinum catalyst. *J. Power Sources* **133**, 145–152.
- Xia, Y.-F., Guo, P., Li, J.-Z., Zhao, L., Sui, X.-L., Wang, Y., and Wang, Z.-B. (2021). How to appropriately assess the oxygen reduction reaction activity of platinum group metal catalysts with rotating disk electrode. *iScience* **24**, 103024.
- Chen, T., Xu, Y., Guo, S., Wei, D., Peng, L., Guo, X., Xue, N., Zhu, Y., Chen, Z., Zhao, B., and Ding, W. (2019). Ternary heterostructural Pt/CNx/Ni as a supercatalyst for oxygen reduction. *iScience* **11**, 388–397.
- Zaman, S., Su, Y.Q., Dong, C.-L., Qi, R., Huang, L., Qin, Y., Huang, Y.-C., Li, F.-M., You, B., Guo, W., et al. (2022). Scalable molten salt synthesis of platinum alloys planted in metal–nitrogen–graphene for efficient oxygen reduction. *Angew. Chem. Int. Ed.* **61**, e202115835.
- Li, Q., Li, L., Yu, X., Wu, X., Xie, Z., Wang, X., Lu, Z., Zhang, X., Huang, Y., and Yang, X. (2020). Ultrafine platinum particles anchored on porous boron nitride enabling excellent stability and activity for oxygen reduction reaction. *Chem. Eng. J.* **399**, 125827.
- Ham, K., Shin, D., and Lee, J. (2020). The role of lone-pair electrons in Pt–N interactions for the oxygen reduction reaction in polymer exchange membrane fuel cells. *ChemSusChem* **13**, 1660–1758.
- Kim, T.-J., Kwon, G., and Kim, Y.-T. (2014). Anomalous increased oxygen reduction reaction activity with accelerated durability test cycles for platinum on thiolated carbon nanotubes. *Chem. Commun.* **50**, 596–598.
- Yang, C.-L., Wang, L.-N., Yin, P., Liu, J., Chen, M.-X., Yan, Q.-Q., Wang, Z.-S., Xu, S.-L., Chu, S.-Q., Cui, C., et al. (2021). Sulfur-anchoring synthesis of platinum intermetallic nanoparticle catalysts for fuel cells. *Science* **374**, 459–464.
- Hu, Y., Zhu, M., Luo, X., Wu, G., Chao, T., Qu, Y., Zhou, F., Sun, R., Han, X., Li, H., et al. (2021). Coplanar Pt/C nanomeshes with ultrastable oxygen reduction performance in fuel cells. *Angew. Chem. Int. Ed.* **60**, 6533–6538.
- Wu, Y.-F., Ma, J.-W., and Huang, Y.-H. (2023). Enhancing oxygen reduction reaction of Pt–Co/C nanocatalysts via synergetic effect between Pt and Co prepared by one-pot synthesis. *Rare Met.* **42**, 146–154.
- Li, M., Zhao, Z., Cheng, T., Fortunelli, A., Chen, C.-Y., Yu, R., Zhang, Q., Gu, L., Merinov, B.V., Lin, Z., et al. (2016). Ultrafine jagged platinum nanowires enable ultrahigh mass activity for the oxygen reduction reaction. *Science* **354**, 1414–1419.
- Luo, M., Zhao, Z., Zhang, Y., Sun, Y., Xing, Y., Lv, F., Yang, Y., Zhang, X., Hwang, S., Qin, Y., et al. (2019). PdMo bimetallic for oxygen reduction catalysis. *Nature* **574**, 81–85.
- Liao, Y., Li, J., Zhang, S., and Chen, S. (2021). High index surface-exposed and composition-graded PtCu<sub>3</sub>@Pt<sub>3</sub>Cu@Pt nanodendrites for high-performance oxygen Reduction. *Chin. J. Catal.* **42**, 1108–1116.
- Zhao, Z., Chen, C., Liu, Z., Huang, J., Wu, M., Liu, H., Li, Y., and Huang, Y. (2019). Pt-based nanocrystal for electrocatalytic oxygen reduction. *Adv. Mater.* **31**, 1808115.
- Huang, L.Y., Edwards, A.O., Tian, X., Wang, Z., Fang, W., and Xia, B.Y. (2021). Advanced platinum-based oxygen reduction electrocatalysts for fuel cells. *Acc. Chem. Res.* **12**, 311–314.
- Xia, Z., Zhu, R., Yu, R., Zhang, S., Jung, J.C.-Y., and Zhang, J. (2022). Review—recent progress in highly efficient oxygen reduction electrocatalysts: from structural engineering to performance optimization. *J. Electrochem. Soc.* **169**, 034512.
- Liu, J., Liu, S., Yan, F., Wen, Z., Chen, W., Liu, X., Liu, Q., Shang, J., Yu, R., Su, D., and Shui, J. (2022). Ultrathin nanotube structure for mass-efficient and durable oxygen reduction reaction catalysts in PEM fuel cells. *J. Am. Chem. Soc.* **144**, 19106–19114.
- Qiao, Z., Wang, C., Zeng, Y., Spendelow, J.S., and Wu, G. (2021). Advanced nanocarbons for enhanced performance and durability of platinum catalysts in proton exchange membrane fuel cells. *Small* **17**, 2006805.
- Chen, J., Ou, Z., Chen, H., Song, S., Wang, K., and Wang, Y. (2021). Recent developments of nanocarbon based supports for PEMFCs electrocatalysts. *Chin. J. Catal.* **42**, 1297–1326.
- Zhang, S., Lu, B., Han, X., Xu, L., Qi, Y., Yin, L., Xu, Y., Zhao, Y., Liu, K., and Peng, J. (2013). Enhanced-electrocatalytic activity of Pt nanoparticles supported on nitrogen-doped carbon for the oxygen reduction reaction. *J. Power Sources* **55**, 60–69.
- Galbiati, S., Morin, A., and Pauc, N. (2015). Nanotubes array electrodes by Pt evaporation: half-cell characterization and PEM fuel cell demonstration. *Appl. Catal. B Environ.* **165**, 149–157.
- Tian, X., Zhao, X., Su, Y.-Q., Wang, L., Wang, H., Dang, D., Chi, B., Liu, H., Hensen, E.J.M., Lou, X.W.D., and Xia, B.Y. (2019). Engineering bunched Pt–Ni alloy nanocages for efficient oxygen reduction in practical fuel cells. *Science* **366**, 850–856.
- Kim, O.-H., Cho, Y.-H., Kang, S.H., Park, H.-Y., Kim, M., Lim, J.W., Chung, D.Y., Lee, M.J., Choe, H., and Sung, Y.-E. (2013). Ordered macroporous platinum electrode and enhanced mass transfer in fuel cells using inverse opal structure. *Nat. Commun.* **4**, 2473.
- Wang, Y., Zhou, Y., Feng, Y., and Yu, X.-Y. (2022). Synergistic electronic and pore structure modulation in open carbon nanocages enabling efficient electrocatalytic production of H<sub>2</sub>O<sub>2</sub> in acidic medium. *Adv. Funct. Mater.* **32**, 2110734.
- Zhang, S., and Chen, S. (2015). Surfactant-template preparation of polyaniline nanotubes for oxygen reduction. *Catalysts* **5**, 1202–1210.
- Chen, M., Chen, J., Jia, C., Luo, J., Yang, Z., Chung-Yen Jung, J., Zhang, J., Chen, S., and Zhang, S. (2023). Metal-free carbon semitubes for oxygen reduction electrocatalysis. *Cell Rep. Phys. Sci.* **4**, 101204.
- Carmo, M., dos Santos, A.R., Poco, J.G., and Linardi, M. (2007). Physical and electrochemical evaluation of commercial carbon black as electrocatalysts supports for DMFC applications. *J. Power Sources* **173**, 860–866.

37. Quinson, J., Inaba, M., Neumann, S., Swane, A.A., Bucher, J., Simonsen, S.B., Theil Kuhn, L., Kirkensgaard, J.J.K., Jensen, K.M.Ø., Oezaslan, M., et al. (2018). Investigating particle size effects in catalysis by applying a size-controlled and surfactant-free synthesis of colloidal nanoparticles in alkaline ethylene glycol: case study of the oxygen reduction reaction on Pt. *ACS Catal.* **8**, 6627–6635.
38. Veith, G.M., Lupini, A.R., Baggetto, L., Browning, J.F., Keum, J.K., Villa, A., Prati, L., Papandrew, A.B., Goenaga, G.A., Mullins, D.R., et al. (2013). Evidence for the formation of nitrogen-rich platinum and palladium nitride nanoparticles. *Chem. Mater.* **25**, 4936–4945.
39. Liu, J., Jiao, M., Lu, L., Barkholtz, H.M., Li, Y., Wang, Y., Jiang, L., Wu, Z., Liu, D.-J., Zhuang, L., et al. (2017). High performance platinum single atom electrocatalyst for oxygen reduction reaction. *Nat. Commun.* **8**, 15938.
40. Stadnichenko, A.I., Muravev, V.V., Koscheev, S.V., Zaikovskii, V.I., Aleksandrov, H.A., Neyman, K.M., and Boronin, A.I. (2019). Study of active surface centers of Pt/CeO<sub>2</sub> catalysts prepared using radio frequency plasma sputtering technique. *Surf. Sci.* **679**, 273–283.
41. Zhang, G., Yang, D., and Sacher, E. (2007). X-ray photoelectron spectroscopic analysis of Pt nanoparticles on highly oriented pyrolytic graphite, using symmetric component line shapes. *J. Phys. Chem. C* **111**, 565–570.
42. Mirsaleh-Kohan, N., Esmaili, S., Bass, A.D., Huels, M.A., and Sanche, L. (2021). Chemical transformation of molecular ices containing N<sub>2</sub>O and C<sub>2</sub>D<sub>2</sub> by low energy electrons: new chemical species of astronomical interest. *J. Chem. Phys.* **154**, 224706.
43. Guo, L., Jiang, W.-J., Zhang, Y., Hu, J.-S., Wei, Z.-D., and Wan, L.-J. (2015). Embedding Pt nanocrystals in N-doped porous carbon/carbon nanotubes toward highly stable electrocatalysts for the oxygen reduction reaction. *ACS Catal.* **5**, 2903–2909.
44. Wang, C., Kuai, L., Cao, W., Singh, H., Zakharov, A., Niu, Y., Sun, H., and Geng, B. (2021). Highly dispersed Cu atoms in MOF-derived N-doped porous carbon inducing Pt loads for superior oxygen reduction and hydrogen evolution. *Chem. Eng. J.* **426**, 130749.
45. Dennany, L., Sherrell, P., Chen, J., Innis, P.C., Wallace, G.G., and Minett, A.I. (2010). EPR characterisation of platinum nanoparticle functionalised carbon nanotube hybrid materials. *Phys. Chem. Chem. Phys.* **12**, 4135–4141.
46. Ham, K., Shin, D., and Lee, J. (2020). The role of lone-pair electrons in Pt-N interactions for the oxygen reduction reaction in polymer exchange membrane fuel cells. *ChemSusChem* **13**, 1660.
47. Guo, D., Shibuya, R., Akiba, C., Saji, S., Kondo, T., and Nakamura, J. (2016). Active sites of nitrogen-doped carbon materials for oxygen reduction reaction clarified using model catalysts. *Science* **351**, 361–365.
48. Cookson, J. (2012). The preparation of palladium nanoparticles. *Platin. Met. Rev.* **56**, 83–98.
49. Zhao, X., Sun, L., Cai, J., Jung, J.C.-Y., Xia, Z., Zhang, J., and Zhang, S. (2022). Facile synthesis of surfactant-induced platinum nanospheres with a porous network structure for highly effective oxygen reduction catalysis. *Chem. Asian J.* **17**, e202200338.
50. An, S., Park, J.-H., Shin, C.-H., Joo, J., Ramasamy, E., Hwang, J., and Lee, J. (2011). Well-dispersed Pd<sub>3</sub>Pt<sub>1</sub> alloy nanoparticles in large pore sized mesocellular carbon foam for improved methanol-tolerant oxygen reduction reaction. *Carbon* **49**, 1108–1117.
51. Yang, Z., Chen, Y., Zhang, S., and Zhang, J. (2023). Identification and understanding of active sites of non-noble iron-nitrogen-carbon catalysts for oxygen reduction electrocatalysis. *Adv. Funct. Mater.* **33**, 2215185.
52. Kim, H., Lee, K., Woo, S.I., and Jung, Y. (2011). On the mechanism of enhanced oxygen reduction reaction in nitrogen-doped graphene nanoribbons. *Phys. Chem. Chem. Phys.* **13**, 17505–17510.
53. Imran Jafri, R., Rajalakshmi, N., and Ramaprabhu, S. (2010). Nitrogen doped graphene nanoplatelets as catalyst support for oxygen reduction reaction in proton exchange membrane fuel cell. *J. Mater. Chem.* **20**, 7114–7117.
54. Yano, H., Watanabe, M., Iiyama, A., and Uchida, H. (2016). Particle-size effect of Pt cathode catalysts on durability in fuel cells. *Nano Energy* **29**, 323–333.
55. Xie, B., Zhang, Y., and Zhang, R. (2017). Coassembly and high ORR performance of monodisperse Pt nanocrystals with a mesopore-rich nitrogen-doped graphene aerogel. *J. Mater. Chem.* **5**, 17544–17548.
56. Holme, T., Zhou, Y., Pasquarelli, R., and O’Hayre, R. (2010). First principles study of doped carbon supports for enhanced platinum catalysts. *Phys. Chem. Chem. Phys.* **12**, 9461–9468.
57. Ma, J., Habrioux, A., Luo, Y., Ramos-Sanchez, G., Calvillo, L., Granozzi, G., Balbuena, P.B., and Alonso-Vante, N. (2015). Electronic interaction between platinum nanoparticles and nitrogen-doped reduced graphene oxide: effect on the oxygen reduction reaction. *J. Mater. Chem.* **3**, 11891–11904.
58. Nørskov, J.K., Rossmeisl, J., Logadottir, A., Lindqvist, L., Kitchin, J.R., Bligaard, T., and Jónsson, H. (2004). Origin of the overpotential for oxygen reduction at a fuel-cell cathode. *J. Phys. Chem. B* **108**, 17886–17892.
59. Giannozzi, P., Baroni, S., Bonini, N., Calandra, M., Car, R., Cavazzoni, C., Ceresoli, D., Chiarotti, G.L., Cococcioni, M., Dabo, I., et al. (2009). Quantum ESPRESSO: a modular and open-source software project for quantum simulations of materials. *J. Phys. Condens. Matter* **21**, 395502.

## STAR★METHODS

### KEY RESOURCES TABLE

REAGENT or RESOURCE	SOURCE	IDENTIFIER
Chemicals, peptides, and recombinant proteins		
H <sub>2</sub> PtCl <sub>6</sub> ·6H <sub>2</sub> O	Titan	18497-13-7
XC-72R	Cabot	1333-86-4
Ethylene glycol	Sinopharm	107-21-1
NaOH	Sinopharm	1310-73-2
HClO <sub>4</sub>	Sinopharm	7601-90-3
KOH	Sinopharm	1310-58-3
Urea	Sinopharm	57-13-6
HCl	Sinopharm	7647-01-0
Nafion solution (5%)	Sigma-Aldrich	31175-20-9
20wt% Pt/C	Johnson Matthey	7440-06-4
Isopropanol	Sinopharm	67-63-0
m-Phenylenediamine	Sinopharm	108-45-2
(NH <sub>4</sub> ) <sub>2</sub> S <sub>2</sub> O <sub>4</sub>	Sinopharm	7775-27-1
Ethanol	Sinopharm	64-17-5
C <sub>16</sub> H <sub>33</sub> (CH <sub>3</sub> ) <sub>3</sub> NBr	Titan	57-09-0

### RESOURCE AVAILABILITY

#### Lead contact

Further information and requests for resources and materials should be directed to and will be fulfilled by the lead contact, Dr. Shiming Zhang ([smzhang@shu.edu.cn](mailto:smzhang@shu.edu.cn)).

#### Materials availability

This study did not generate new unique reagents.

#### Data and code availability

- Data reported in this paper will be shared by the [lead contact](#) upon request.
- This paper does not report original code.
- Any additional information required to reanalyze the data reported in this paper is available from the [lead contact](#) upon request.

### METHOD DETAILS

#### Preparation of N-CST support

For a typical preparation process, 5.83 g of cetyl trimethyl ammonium bromide (CTAB) was dissolved into 75 mL of ultrapure water. Thereafter, 1 g of m-phenylenediamine (mPDA) and 100 mL of 1 M HCl were consecutively added under sonication for 30 minutes to obtain the precursor solution. Then, 25 mL of ammonium persulfates (APS) solution (0.4 M) was added into the precursor solution to trigger the polymerization of mPDA at room temperature for 24 hours. The brownish black precipitate was collected by centrifugation, and further washed by ethanol and water for three times followed by freeze-drying. Then, the obtained carbon semi-tube (CST) product was heated at 900 °C for 3 hours in an Ar flow and the resultant support material of N-doped CST was denoted as N-CST.

#### Synthesis of Pt/N-CST catalyst

The synthesis of Pt nanoparticles (NPs) was implemented by an ethylene glycol (EG) thermal reduction method. Typically, 2 mL of NaOH/EG solution (0.4 M) and 2 mL of H<sub>2</sub>PtCl<sub>6</sub>·6H<sub>2</sub>O/EG solution (38.6 mM)

were mixed in a 25 mL glass flask, and the mixture was treated for 2 minutes at 160 °C and 160 W in a microwave reactor. To purify the Pt NPs, 15 mL of 1 M HCl was added to the black suspension and centrifuged three times. Then, the residual Pt NPs suspension was mixed with the N-CST support by dispersing them into 5 mL of ethanol with ultrasonication for 1.5 hours. The centrifugal product was washed with ultrapure water and then dried at 80 °C overnight to obtain the final 20 wt% Pt/N-CST catalyst.

### Physical characterizations

Transmission electron microscopy (TEM) and high-resolution TEM (HRTEM) were conducted on a JEOL JEM-F200 at an acceleration voltage of 200 kV. Scanning electron microscopy (SEM) images were obtained by Nova Nano SEM 450. The high-angle annular dark-field scanning transmission electron microscopy (HAADF-STEM) images of samples were observed on a JEOL JEM-F200 microscope with an accelerating voltage of 200 keV. X-ray diffraction (XRD) patterns were characterized by D/MAX2200 at the voltage of 40 kV and the current of 40 mA using Cu K $\alpha$  radiation ( $\lambda = 0.15406$  nm). X-ray photoelectron spectroscopy (XPS) analysis was performed on the Thermo Scientific K-Alpha and all the binding energy values have been calibrated with reference to the C1s peak at 284.8 eV. Nitrogen (N<sub>2</sub>) adsorption-desorption isotherms were recorded with an ASAP 2460 instrument (Micromeritics, USA). The electron paramagnetic resonance (EPR) spectroscopy was measured on Bruker EMX PLUS, with typical set parameters that the resonance frequency was 9.8259 GHz, the attenuator was 20.0 dB, the sweep width was 6000 G, the modulation frequency was 100 kHz, the modulation amplitude was 4 G, and the scan time was 30 s.

### Electrochemical measurements

All the electrochemical measurements of the as-prepared samples were performed on a CHI electrochemical workstation (CHI 760e) in a conventional three-electrode cell with a Pt foil as the counter electrode. And, the saturated calomel electrode (SCE) and mercury/mercury oxide (Hg/HgO) electrode were used as reference electrodes in acidic (0.1 M HClO<sub>4</sub>) and alkaline (0.1 M KOH) electrolytes. All the measured potentials were converted to the reversible hydrogen electrode (RHE). The catalyst ink was prepared by dispersing 5 mg 20 wt% Pt/N-CST catalyst in 1 mL isopropanol solution containing Nafion (Nafion : isopropanol = 1 : 48) under sonication for 30 minutes. 6  $\mu$ L of the above ink was drop-casted onto the glass carbon (GC) disk electrode (5 mm diameter) to make the working electrode with a total Pt loading of 30  $\mu$ g<sub>Pt</sub> cm<sup>-2</sup>. For comparison, 20 wt% Pt/C catalyst (Johnson Matthey Corporation) was used as the baseline for comparison. The catalyst loadings were controlled at 0.15 mg cm<sup>-2</sup> for the various Pt catalysts (30  $\mu$ g<sub>Pt</sub> cm<sup>-2</sup>) and 0.4 mg cm<sup>-2</sup> for the N-CST and XC-72R supports. Cyclic voltammetry (CV) was carried out in a N<sub>2</sub>-saturated 0.1 M HClO<sub>4</sub> solution with a scanning rate of 50 mV s<sup>-1</sup>. The catalytic ORR activity tests were performed by linear sweep voltammetry (LSV) in an O<sub>2</sub>-saturated electrolyte through the RDE method at 10 mV s<sup>-1</sup> and 1600 rpm. The kinetic current density ( $j_k$ ) was calculated from the mass-transport correction based on the Koutecký–Levich equation:

$$\frac{1}{j} = \frac{1}{j_k} + \frac{1}{j_d} \quad (\text{Equation 1})$$

where,  $j$  is the measured current density,  $j_k$  is the current density and  $j_d$  is the limiting diffusion current density.

The accelerated durability test (ADT) was performed in the O<sub>2</sub>-saturated 0.1 M HClO<sub>4</sub> electrolyte by potential cycling between 0.6 and 1.1 V (vs. RHE) with a scan rate of 100 mV s<sup>-1</sup> for 10000 cycles.

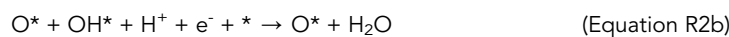
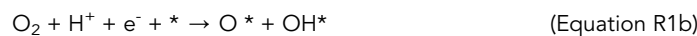
### DFT calculations

#### DFT parameters

All calculations were carried out using the Plane-Wave Self-Consistent Field (PWSCF) codes included in the Quantum ESPRESSO distribution.<sup>59</sup> The spin-polarized density functional theory (DFT) calculations were performed with periodic supercells utilizing the generalized gradient approximation (GGA) and the Perdew-Burke-Ernzerhof (PBE) exchange-correlation functional, as well as ultrasoft pseudopotentials for both nuclei and core electrons. The Kohn-Sham orbitals were expanded in a plane-wave basis set with a kinetic energy cutoff of 30 Ry and a charge-density cutoff of 300 Ry. The Fermi-surface effects were taken into account by applying the Methfessel and Paxton smearing technique, with a smearing parameter of 0.02 Ry. The various graphene doping structures were modeled using periodic supercells consisting of single-layer graphene, with a 20 Å vacuum above.

### Details for free energy diagram and adsorption energies calculations

The reaction mechanisms for ORR are written as follows:



Note: the alternative of R1a and R1b, and that of R2a and R2b will take place.

To calculate the free energy diagrams from R1 to R5, we employed the classical computational hydrogen electrode (CHE) method to treat the free energies of protons and electrons.<sup>58</sup> The associated adsorption free energies of the adsorbates were determined using the following expression:

$$G_A = E_A + \text{ZPE} - TS + \int C_p dT \quad (\text{Equation R5})$$

where,  $E_A$  is the total energy of a certain molecule A or adsorbate  $A^*$ . For molecule,  $E_A$  can be obtained directly through a gas phase calculation; For a certain adsorbate,  $E_A$  is calculated by the difference between the DFT based substrate with ( $E_{A^*}^{\text{DFT}}$ ) and without adsorbate A ( $E_*^{\text{DFT}}$ ):

$$E_A = E_{A^*}^{\text{DFT}} - E_*^{\text{DFT}} \quad (\text{Equation R6})$$

where, ZPE,  $TS$  and  $\int C_p dT$  are the correction from zero point energy, entropy and heat capacity, whose values are listed in Table S2. Other than that,  $\text{H}^+$  is calculated by the Gibbs free energy of  $1/2\text{H}_2$ , and the energy of electron is calculated by  $-U_e$ .

### The computational hydrogen electrode (CHE) method

Generally, when studying electrocatalytic reactions using first-principles methods, two challenges must be addressed: calculating the reaction barrier for the proton-coupled electron transfer (PCET) process and determining the Gibbs free energy of solvated  $\text{H}^+$ . The CHE method, proposed by Norskov et al.<sup>58</sup>, provides a means of circumventing these challenges. Within the framework of the CHE method, the reaction in question can be represented as follows:



reaches equilibrium on  $U_{\text{SHE}} = 0 \text{ V}$ , one can replace the energy of  $\text{H}^+$  with that of  $1/2\text{H}_2$ :

$$G_{\text{H}^+} = 1/2G_{\text{H}_2} \quad (\text{Equation R8})$$

The energy of the electron can be denoted as  $-U_e$ , where  $U$  is the electrode potential relative to the standard hydrogen electrode (SHE). With regards to the PCET reaction barrier, the CHE method assumes that the overpotential of the electrocatalytic reaction is the minimum overpotential required to ensure that the standard Gibbs free energies of all elementary steps are exothermic. This potential is referred to as the reaction-limiting potential ( $U_l$ ). In practice,  $U_l$  can serve as an activity descriptor and can be used to determine the exact reaction pathway, particularly for reactions such as the ORR.